Linear viscoelasticity of hard sphere colloidal crystals from resonance detected with dynamic light scattering

See-Eng Phan, Min Li, and William B. Russel
Department of Chemical Engineering, Princeton University, Princeton, New Jersey 08544

Jixiang Zhu and Paul M. Chaikin
Department of Physics, Princeton University, Princeton, New Jersey 08544

Chris T. Lant
NYMA, 2001 Aerospace Parkway, Brook Park, Ohio 44142

(Received 28 April 1998; revised manuscript received 28 January 1999)

We present measurements of the high-frequency shear modulus and dynamic viscosity for nonaqueous hard sphere colloidal crystals both in normal and microgravity environments. All experiments were performed on a multipurpose PHaSE instrument. For the rheological measurements, we detect the resonant response to oscillatory forcing with a dynamic light scattering scheme. The resonant response for colloidal crystals formed in normal and microgravity environments was similar, indicating that the bulk rheological properties are unaffected by differing crystal structure and crystallite size within the experimental error. Our high-frequency shear modulus seems reasonable, lying close to Frenkel and Ladd's predictions [Phys. Rev. Lett. **59**, 1169 (1987)] for the static modulus of hard sphere crystals. Our high-frequency dynamic viscosity, on the other hand, seems high, exceeding Shikata and Pearson [J. Rheol. **38**, 601 (1994)] and van der Werff *et al.*'s measurements [Phys. Rev. A **39**, 795 (1989)] on the high-frequency dynamic viscosity for metastable fluids. The measurements are in the linear regime for the shear modulus but may not be for the dynamic viscosity as Frith *et al.* [Powder Technol. **51**, 27 (1987)] report that the dynamic viscosity passes through a maximum with strain amplitude. [S1063-651X(99)08708-5]

PACS number(s): 82.70.Dd, 83.50.Fc

I. INTRODUCTION

Concentrated colloidal dispersions occur in a wide range of everyday products such as paper, paints, plastics, soaps, medicines, and ceramics. The simplest colloidal dispersion consists of hard spheres, which interact through hydrodynamic and Brownian forces but feel no direct force before an infinite repulsion at contact. The hard sphere phase diagram, including the disorder-order transition, has been well established [1], as has the rheology in the dilute fluid phase [2]. Many-body interactions, however, complicate the understanding of the transport properties at higher concentrations in both disordered/metastable fluids and the ordered solid.

Previous studies examined the rheological properties under both steady [3–5] and oscillatory shear [6–9] for hard sphere fluids, below the freezing transition and in the metastable region above. Many rheological studies also exist for colloidal crystals, but focus on aqueous dispersions affected by electrostatic forces under both steady [10,11] and oscillatory shear [12–15]. The main difficulty in determining the elasticity is that colloidal crystals are orders of magnitude weaker than conventional atomic solids and, thus, easily melt under shear. The weakness of the elastic forces results from the low number density, which for our colloidal crystals is ~ 4 per cubic micron compared with ~ 1 per cubic angstrom for atomic solids. The static elastic constants reflect the energy density and may be estimated as the interparticle energy times the number density. At room temperature, the interparticle energies are comparable for colloidal and atomic crystals and, therefore, the elastic constants for colloidal crystals should be $\sim 10^{12}$ times weaker. Oscillatory shear of small amplitude slightly perturbs the microstructure and is suitable for measuring the linear viscoelasticity of colloidal crystals.

This work extends rheological measurements for colloidal crystals to nonaqueous hard sphere dispersions. Similar to previous studies on aqueous dispersions, described below, we excite shear waves in our samples and then implement a novel detection scheme using dynamic light scattering to measure the resonant response. From that information, we can extract the shear modulus and dynamic viscosity. Since no other measurements exist for nonaqueous hard spheres, we compare our results with the available theory for a face-centered cubic (fcc) hard sphere crystal and measurements on the metastable hard sphere fluid. In addition to measurements in the lab, experiments were performed in microgravity on NASA space shuttle missions STS-83 and STS-94. We can therefore compare the results obtained in gravity and microgravity environments.

The first few sections of this work provide background on dynamic rheological measurements, resonant techniques used to determine the viscoelasticity of charged colloidal crystals, and predictions of the viscoelastic properties of hard sphere fcc crystals. We then describe our hard sphere colloidal crystals, experimental method, and theoretical model for determining the shear modulus and dynamic viscosity from the measured resonant response. Finally, we present our results and end with a discussion.

II. DYNAMIC RHEOLOGICAL MEASUREMENTS

In equilibrium, Brownian motion and the hard sphere repulsion determine the particle distribution. A weak oscilla-

tory shear perturbs the distribution from equilibrium and generates elastic and dissipative responses. The elasticity arises from the interparticle potential and Brownian motion, which counteract the external flow field and tend to restore the microstructure to equilibrium. The dissipation originates from viscous stresses in the medium surrounding the particles and relaxation of the microstructure.

For small amplitude oscillations with frequency ω, the local stress and strain are related through the complex shear modulus

$$G^*(\omega)=i\omega\eta^*(\omega)=G'(\omega)+iG''(\omega), \tag{2.1}$$

where $\eta^*(\omega)$ is the complex shear viscosity and $G'(\omega)$ and $G''(\omega)$ characterize the components of the stress in phase and out of phase with the applied strain, respectively. At zero frequency, the stress for a fluid is completely in phase with the applied rate of strain and determines the low shear limiting viscosity η_o,

$$\lim_{\omega\to 0}\frac{G''(\omega)}{\omega}=\eta_o. \tag{2.2}$$

Crystals have long-range positional order, which results in Bragg rings and a finite static shear modulus G_o,

$$\lim_{\omega\to 0}G'(\omega)=G_o, \tag{2.3}$$

which vanishes at the melting transition. These features distinguish crystals from fluids, which have no long-range positional order. In the high-frequency limit, the in- and out-of-phase components give the high-frequency dynamic viscosity η'_∞ and high-frequency shear modulus G'_∞, respectively,

$$\lim_{\omega\to\infty}\frac{G''(\omega)}{\omega}=\eta'_\infty, \tag{2.4}$$

$$\lim_{\omega\to\infty}G'(\omega)=G'_\infty. \tag{2.5}$$

Presumably G'_∞ and η'_∞ both diverge for monodisperse spheres at close packing ($\phi=0.74$). The loss tangent $\tan\delta=G''/G'$ shows the transition from viscous ($\tan\delta>1$) to elastic ($\tan\delta<1$) behavior.

A. Rheology of charged colloidal crystals

Previous studies on the viscoelasticity of colloidal crystals center on aqueous polystyrene lattices. Ordering of aqueous dispersions depends on the number density, particle size, and electrolyte concentration. One of the first measurements of the bulk modulus of colloidal crystals by Crandall and Williams [16] detected the gravitational compression of the crystal lattice as a function of height for dilute dispersions by Bragg scattering and extracted Young's modulus. Because of the extremely long time required to reach equilibrium for gravitational compression and the desire to determine the shear modulus rather than the bulk modulus, other groups [17,18] excited standing shear waves in a cylinder filled with opaque dispersions and detected the amplitude and phase from Kossel rings to construct a resonant curve. Joanny [19] solved the equation of motion to obtain the resonance frequencies and also determined that only low-frequency shear modes propagate in a cylinder of charged colloidal crystals. Knowing this, Dubois-Violette *et al.* [17] deduced the shear modulus and dynamic viscosity from their resonant curve. Mitaku *et al.* [20,21] employed a slight variation on this technique, detecting the resonances mechanically instead of from Kossel rings. Many investigators [12,13,22–24] used custom rheometers with mechanical detection schemes at a fixed frequency to determine the increase in the shear modulus of colloidal crystals with increasing concentration and decreasing particle size and electrolyte concentration.

van der Vorst *et al.* [15,25] determined the frequency dependence of the storage and loss modulus of charged colloidal crystals with particle radius $a=2.45\times10^{-7}$ m and nearest-neighbor distances r_{nn} between $2.7a$ and $7.3a$ using a variety of rheometers. These measurements cover dimensionless frequencies $(L_m r_{nn})^2\omega/D_o$ from 1.4×10^{-4} to 1.3×10^5, scaled with the Lindemann criterion at melting $L_m=0.15$ and the Stokes-Einstein diffusion coefficient D_o. For $(L_m r_{nn})^2\omega/D_o<0.9$, the storage modulus for volume fractions $\phi>0.10$ is nearly constant, only increasing 10% for dimensionless frequencies from 1.4×10^{-4} to 0.9, while the loss modulus passes through a minimum and is at least an order of magnitude smaller ($\tan\delta<1.0$). At higher dimensionless frequencies [for $\phi=0.2$, $(L_m r_{nn})^2\omega/D_o>9.0$], the storage modulus remains close to the static modulus but with large error bars, while the loss modulus increases linearly with frequency and eventually exceeds the storage modulus, as in the fluid case. The viscosity in the high-frequency limit is approximately the medium viscosity. Scaling their results and others for the static shear modulus with volume fraction, particle radius, surface charge density, and electrolyte concentration yields a master curve with some scatter. Storage and loss moduli of Blom *et al.* [26] follow similar trends, but indicate a stronger frequency dependence for the storage modulus.

Palberg *et al.* [27] accurately ($\Delta G\leqslant 2\%$) and nondestructively determined the shear modulus of charged colloidal crystals by detecting resonant shear oscillations with time-resolved static light scattering. With transparent samples, they determined the morphology and then placed a position-sensitive detector on part of a Bragg ring and measured the change in Bragg angle due to the distortion of the lattice. For small-amplitude oscillations, the periodic distortion of the lattice spacing reflects the response of the crystallite to the forcing. They found the shear modulus to be sensitive to different bcc crystal morphologies; at 0.5 μmol/l salt, $G'=0.34$ Pa for an unoriented polycrystal, $G'=0.30$ Pa for an unoriented polycrystalline core with twinned monocrystal outer annulus, and $G'=0.23$ Pa for an oriented polycrystal. Theories based on electrostatic interactions agree with measurements of the shear moduli of these colloidal crystals by the various resonant techniques [28–30]. Thus, understanding of the elasticity of charged colloidal crystals is well advanced.

B. Theory on rheology of hard sphere colloidal crystals

Predictions of the viscoelasticity of hard sphere crystals are limited. Frenkel and Ladd [31] computed the static elas-

tic constants C_{ij} from molecular-dynamics simulations of slightly distorted unit cells at several concentrations and then averaged over all orientations to obtain the static shear modulus for an isotropic polycrystalline solid,

$$G_o=\frac{1}{5}[C_{11}-C_{12}+3C_{44}]. \tag{2.6}$$

Nunan and Keller [32] calculated the effective viscosity of periodic arrays of spheres in an incompressible Newtonian fluid with viscosity μ. For a cubic lattice, the effective viscosity tensor involves just two parameters, α and β, which are functions of concentration and the lattice geometry. The orientational averaged effective viscosity, which corresponds to the high-frequency limit for a perfect crystal, follows as

$$\eta'_\infty=\mu\left[1+\frac{1}{5}(2\alpha+3\beta)\right]. \tag{2.7}$$

Our particles undergo Brownian fluctuations about the lattice point, whereas Nunan and Keller assumed the particles to be fixed on the lattice, reducing the radial distribution function $g(r)$ at contact to zero. As evidenced by the osmotic pressure, which is proportional to $g(r)$ at contact, a significant number of nearest-neighbor interactions exist, implying that Eq. (2.7) should represent a lower bound on η'_∞ for a colloidal crystal.

III. RESONANT BEHAVIOR

Similar to the investigations on charged colloidal crystals, we exploit resonant behavior to determine both the shear modulus and dynamic viscosity of our hard sphere colloidal crystals. Our dispersions have inertia (density), damping (dynamic viscosity), and recovery (shear modulus), the combination of which governs the amplitude of the response relative to the amplitude of the forcing. For a small dynamic viscosity, the amplitude of the response becomes large at a series of discrete (resonant) frequencies and characterization of the first resonance suffices to determine the dynamic viscosity and shear modulus. Instead of measuring the change in the Bragg angle as Palberg *et al.* [27] did or determining the amplitude and phase from Kossel rings as did Dubois-Violette *et al.* [17] and Joanicot *et al.* [18], we detect the resonant response with dynamic light scattering, since the decay of the autocorrelation function also reflects the amplitude of the response.

A. PMMA-PHSA spheres

Ottewill and his group at the University of Bristol synthesized and graciously supplied samples of poly-(methyl methacrylate) (PMMA) spheres with a grafted comblike layer of poly-(12-hydroxy stearic acid) (PHSA) chains that we dispersed in a refractive index matching mixture of 1,2,3,4-tetrahydronapthalene (tetralin, $n=1.541$) and 1,2,3,4-*cis*-decahydronapthalene (decalin, $n=1.4815$). Tetralin is a good solvent for PMMA and swells the particles, significantly increasing the size [33]. Index matching suppresses the van der Waals forces and is necessary for performing light scattering, but the associated swelling increases the effective hard sphere volume fraction ϕ. The particle diameter from dynamic light scattering on a dilute sample is $2a=655\pm15$ nm. Previous measurements of the equation of state demonstrate them to be near hard spheres [34] with the effective hard sphere size determined by matching the observed disorder-order transition to the hard sphere freezing transition. Polydispersity affects the freezing transition [35], but the error in determining the concentration (±0.007) exceeds the correction for the 5% polydispersity of our samples. Thus, the effective volume fractions reported here do not include the correction for polydispersity.

Index matching does not lead to density matching; the resulting sedimentation can affect both the structure and size of the crystallites [36]. Face-centered cubic (fcc) is entropically favored over hexagonal close packing (hcp), a conclusion advanced by Woodcock [37] on the basis of simulations and confirmed by Bolhuis *et al.* [38] through further analysis. Under normal gravity, hard sphere dispersions crystallize into a mixture of hcp and fcc packing with a bias towards fcc [39], whereas under microgravity, only random hexagonal close packing (rhcp) structure has been detected [36]. The structural difference may result from gravity-induced stresses. In addition, samples in the coexistence region under microgravity form larger crystallites than in normal gravity and also exhibit dendritic growth [40]. Both crystal structure and crystallite size may affect the rheological properties, motivating a comparison of results obtained in normal and microgravity environments.

B. Experimental setup

A multipurpose light scattering instrument shown in Fig. 1 was designed by NASA Lewis Research Center, ADF Corporation, NYMA Corporation, Titan Spectron, and Princeton University for the Physics of Hard Sphere Experiments or PHaSE [41]. This instrument performs both static and dynamic light scattering and also oscillates the sample for determining the rheological properties. Specially designed glass sample cells, whose refractive index ($n=1.511$) matches that of our PMMA-PHSA suspensions, consist of two pieces, a face plate and a hemispherical cap. The cap has a parabolic skirt and a cylindrical cavity, 1.0 cm in radius and 1.0 cm high, that requires approximately 3 mL of sample. The face plate is screwed into the cap to seal the sample. To allow for expansion and contraction due to temperature fluctuations, we incorporate a rubber diaphragm in the sample cell. All surfaces of the sample cell are highly polished and coated with antireflective material.

A 100 mW Adlas diode laser Model DPY 313II supplies a $\lambda=532$ nm green beam, which is split into two, one for static light scattering and the other for dynamic. Each beam is routed with Newport mirrors and holders into single mode, polarization maintaining (PM) fiber optic cables terminated on both ends with a quarter-pitch gradient index (GRIN) lens. The GRIN lens restricts the *k* vector of the collected light and focuses the beam to a 100 μm Gaussian waist. The static launch fiber couples with a collimator that delivers a wide beam axially through the sample cell's face plate. The diffracted intensity from the sample is focused without distortion by the hemispherical cap onto a fluorescently coated spherical screen. A high-resolution charge coupled device (CCD) captures a 1032×1312 pixel black and white image

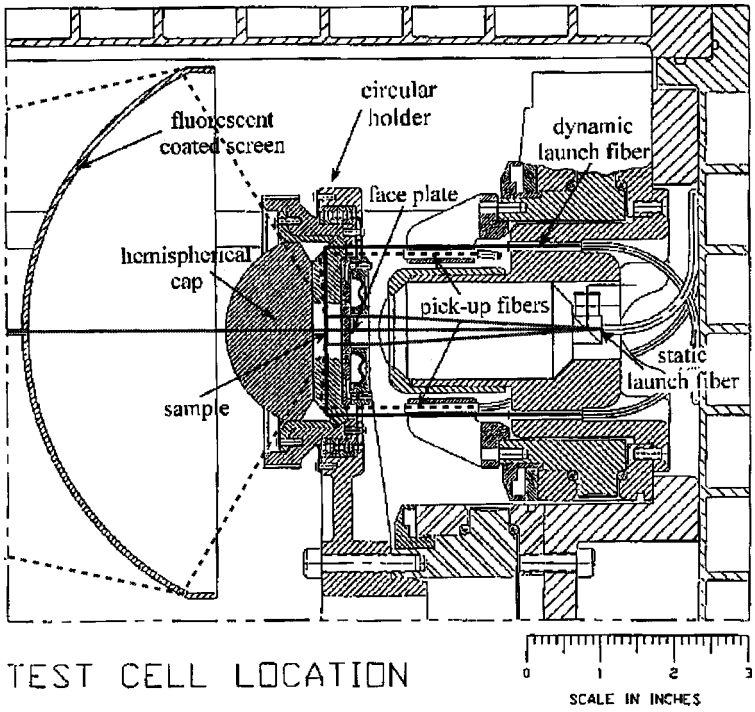

FIG. 1. Schematic diagram of the PHaSE instrument. This instrument performs static and dynamic light scattering and also oscillates the sample cell sinusoidally to determine the rheology. The thick black and gray lines refer to the dynamic and static laser beams, respectively (——, incident beam; — — —, scattered beam).

of the screen containing 2D diffraction images from 0.5° to 60°. For a crystal, the intensity will constructively interfere and result in Bragg rings with positions and intensities that reflect the crystal structure.

The dynamic launch fiber is mounted on a precision stage for directing the beam onto the parabolic skirt and through the center of the cell. The beam is totally internally reflected from the skirt radially through the sample; therefore, the beam from the dynamic launch fiber is perpendicular to that from the Bragg launch fiber. The two single-mode pick-up fibers, 180° apart, are attached to a motorized stage, allowing the scattered intensity to be collected at angles $\theta=10°-169°$ with 0.1° resolution. A supersensitive avalanche photodiode detector (APD) converts the scattered intensity into binary data from which two Brookhaven BI9000 correlators compute autocorrelation functions.

The sample cell is mounted into a circular holder, whose outer edge has ridges that grip a rubber belt that also hugs the gear of a PMI ServoDisc dc motor. The motor transmits sinusoidal oscillations at frequencies between 0.2 and 5 Hz to the sample cell through the rubber belt. Because our samples crystallize and, thus, are nonergodic, we ensemble-average by rotating the cell slowly ($<1°$ in a minute) through many configurations.

C. Viscoelastic solid cylinder in oscillatory shear

Our rheological measurement is nonviscometric, imposing periodic oscillations on the sample cell and detecting the response that propagates through the viscoelastic medium to the center of the cell. Hence the measured response must be compared with predictions from a faithful model in order to identify the shear modulus G' and dynamic viscosity η'. This requires solving the equations of motion for a viscoelastic solid contained in a circular cylinder of radius R and height L that rotates periodically with frequency ω and amplitude γ about its axis. In standard cylindrical coordinates, the only displacement excited by this oscillatory shear is in the azimuthal or θ direction, i.e., u_θ, and pressure gradients are zero, leaving

$$\rho\frac{\partial^2 u_\theta}{\partial t^2}=\left(G'+\eta'\frac{\partial}{\partial t}\right)\left[\frac{\partial}{\partial r}\left(\frac{1}{r}\frac{\partial(ru_\theta)}{\partial r}\right)+\frac{\partial^2 u_\theta}{\partial z^2}\right], \quad (3.1)$$

where ρ is the dispersion density, t is the time, and r and z are the radial and axial positions within the cylinder. This balance between inertia and mechanical stresses determines the propagation of motion into the sample from the boundaries, which rotate as a rigid body. In the low-frequency limit one expects solid body rotation of the entire sample, while at very high frequency inertia should maintain the bulk of the sample at rest with deformation confined to boundary layers near the container walls.

To simplify the analysis, we subtract the solid body rotation from the actual displacement and separate the oscillatory dependence on time as $u_\theta=(\bar{u}_\theta R+\gamma r)e^{i\omega t}$, so that the no-slip boundary conditions at the container walls will be homogeneous for $\bar{u}_\theta$. The behavior then depends on the dimensionless position, $\bar{r}=r/R$ and $\bar{z}=z/R$, the reduced frequency

$$\Omega=\omega R\sqrt{\frac{\rho}{G'}}, \quad (3.2)$$

the reduced viscosity

$$\zeta=\frac{\eta'}{R\sqrt{\rho G'}}, \quad (3.3)$$

and a convenient combination of the two,

$$\sigma=\sqrt{\frac{\Omega^2}{1+i\zeta\Omega}}. \quad (3.4)$$

The dimensionless, time-independent equation for $\bar{u}_\theta$,

$$-\sigma^2(\bar{u}_\theta+\gamma\bar{r})=\frac{\partial}{\partial\bar{r}}\left(\frac{1}{\bar{r}}\frac{\partial(\bar{r}\bar{u}_\theta)}{\partial\bar{r}}\right)+\frac{\partial^2\bar{u}_\theta}{\partial\bar{z}^2}, \tag{3.5}$$

is subject to the no-slip and symmetry boundary conditions

$$\text{at}\quad \bar{z}=0,\quad \bar{u}_\theta=0,$$

$$\text{at}\quad \bar{z}=h,\quad \bar{u}_\theta=0,$$

$$\text{at}\quad \bar{r}=1,\quad \bar{u}_\theta=0,$$

$$\text{at}\quad \bar{r}=0,\quad \bar{u}_\theta=0,$$

where $h=L/R$ is the aspect ratio of the container.

We separate variables

$$\bar{u}_\theta=\sum_{n=1}^{\infty} R_n(\bar{r})Z_n(\bar{z}), \tag{3.6}$$

reducing the partial differential equation to two ordinary differential equations, and obtain first-order Bessel functions of the first and second kind for $R_n(\bar{r})$ and hyperbolic functions for $Z_n(\bar{z})$ with

$$R_n(\bar{r})=A_nJ_1(\Gamma_n\bar{r})+B_nY_1(\Gamma_n\bar{r}). \tag{3.7}$$

The third and fourth boundary conditions yield $B_n=0$ and $J_1(\Gamma_n)=0$ and orthogonormality yields the homogeneous eigenfunction

$$R_n(\bar{r})=\frac{\sqrt{2}}{J_2(\Gamma_n)}J_1(\Gamma_n\bar{r}). \tag{3.8}$$

Solving the z-dependent ODE,

$$\sum_{n=1}^{\infty}\bar{r}R_n\frac{\partial^2Z_n}{\partial\bar{z}^2}=\sum_{n=1}^{\infty}Z_n\left[-\frac{\partial}{\partial\bar{r}}\left(\bar{r}\frac{\partial R_n}{\partial\bar{r}}\right)-\left(\sigma^2\bar{r}-\frac{1}{\bar{r}}\right)R_n\right]-\sigma^2\gamma\bar{r}^2, \tag{3.9}$$

by expanding the nonhomogeneous term in the eigenfunctions R_n and applying the first two boundary conditions leads to

$$Z_n(\bar{z})=\sum_{n=1}^{\infty}\frac{\sqrt{2}\sigma^2\gamma}{\Gamma_n}\left(1-\cosh\lambda_n\bar{z}+\frac{(\cosh\lambda_nh-1)}{\sinh\lambda_nh}\sinh\lambda_n\bar{z}\right) \tag{3.10}$$

with $\lambda_n=\sqrt{\Gamma_n^2-\sigma^2}$.

Combining the r-dependent and z-dependent solutions results in the full solution

$$\frac{u_\theta}{\gamma R}=\bar{r}e^{i\omega t}+\sum_{n=1}^{\infty}\frac{2\sigma^2J_1(\Gamma_n\bar{r})}{\lambda_n^2\Gamma_nJ_2(\Gamma_n)}\left[1-\cosh\lambda_n\bar{z}+\frac{(\cosh\lambda_nh-1)}{\sinh\lambda_nh}\sinh\lambda_n\bar{z}\right]e^{i\omega t}. \tag{3.11}$$

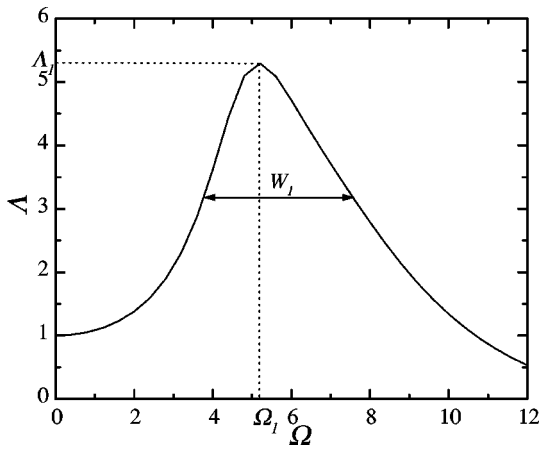

FIG. 2. Typical response to oscillatory shear from model with frequency-independent rheological properties vs driving frequency at $r=0$, $h=1.0$, and $\zeta=0.10$.

A more convenient form results from the identity

$$\bar{r}+\sum_{n=1}^{\infty}\frac{2\sigma^2J_1(\Gamma_n\bar{r})}{\lambda_n^2\Gamma_nJ_2(\Gamma_n)}=\frac{J_1(\sigma\bar{r})}{J_1(\sigma)} \tag{3.12}$$

as

$$\frac{u_\theta}{\gamma R}=\frac{J_1(\sigma\bar{r})}{J_1(\sigma)}e^{i\omega t}+\sum_{n=1}^{\infty}\frac{2\sigma^2J_1(\Gamma_n\bar{r})}{\lambda_n^2\Gamma_nJ_2(\Gamma_n)}\left[\frac{(\cosh\lambda_nh-1)}{\sinh\lambda_nh}\sinh\lambda_n\bar{z}-\cosh\lambda_n\bar{z}\right]e^{i\omega t}. \tag{3.13}$$

We measure the amplitude of angular rotation at the center of the cylinder ($\bar{r}=0$, $\bar{z}=h/2$),

$$\Lambda(\omega)e^{i\omega t}\equiv\frac{1}{\gamma}\frac{\partial u_\theta}{\partial r}=\left[\frac{\sigma}{2J_1(\sigma)}-\sum_{n=1}^{\infty}\frac{\sigma^2}{\lambda_n^2J_2(\Gamma_n)}\times\left(\frac{1}{\cosh\lambda_n\frac{h}{2}}\right)\right]e^{i\omega t}, \tag{3.14}$$

with resonances defined by maxima in Λ. Fig. 2 shows a typical response for a given ζ, indicating three important characteristics of the first resonance, the amplitude Λ_1, position Ω_1, and the width at half height W_1. The typical dimensionless viscosity measured for our hard sphere crystals indicates $\zeta=0.10$, which suppresses the higher-order resonances. The width is calculated relative to the maximum amplitude minus one (an arbitrary baseline). Knowing two of these three characteristics specifies the shear modulus and dynamic viscosity of the dispersion.

In Fig. 3, we plot the amplitude, position, and width of the first resonance for the finite cylinder ($h=1.0$) as a function of dimensionless viscosity. As expected, the amplitude of the first resonance decreases with increasing viscosity, while the position passes through a maximum and decreases and the width broadens. The extrema result from the second reso-

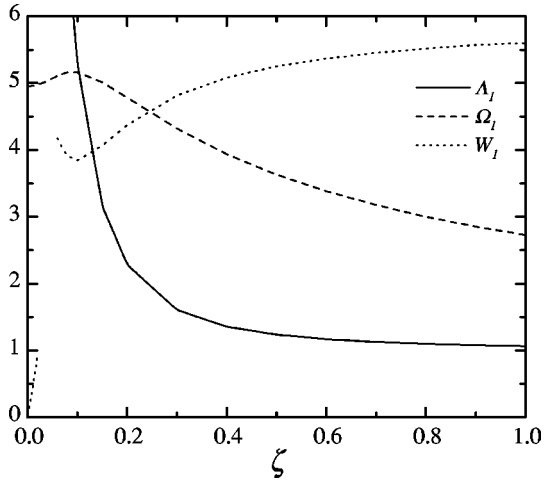

FIG. 3. The amplitude, position, and width at half peak height of the first resonance vs ζ for finite cylinder of a viscoelastic solid in oscillatory shear at $r=0$ and $h=1.0$.

nance merging with the first, which prevents some values for the width from being obtained.

IV. DYNAMIC LIGHT SCATTERING

In dynamic light scattering, the detector measures the instantaneous scattered intensity $I(q,t)=E(q,t)E^*(q,t)$, with $E(q,t)$ the scattered electric field and $E^*(q,t)$ its complex conjugate, of a single fluctuating speckle at a wave vector of magnitude

$$q=\frac{4\pi n}{\lambda}\sin\frac{\theta}{2}. \tag{4.1}$$

A correlator accumulates the intensity over short time periods and constructs a normalized scattered intensity autocorrelation function

$$g_2(q,\tau)=\frac{\langle I(q,0)I(q,\tau)\rangle}{\langle I(q,0)\rangle^2}, \tag{4.2}$$

where the angular brackets represent an ensemble average and τ the delay time. To explicitly relate $g_2(q,\tau)$ to particle positions $\boldsymbol{r}_i(t)$, we invoke the Siegert relationship

$$g_2(q,\tau)=1+Cg_1^2(q,\tau), \tag{4.3}$$

where $C=O(1)$ is an apparatus constant related to the ratio of the detector and coherence areas. The normalized scattered electric field autocorrelation function $g_1(q,\tau)$ or the coherent intermediate scattering function is given by

$$g_1(q,\tau)=\frac{\langle E(q,0)E^*(q,\tau)\rangle}{\langle I(q,0)\rangle}=\frac{1}{NS(q)}\sum_{i,j=1}^{N}\langle\exp\{i\boldsymbol{q}\cdot[\boldsymbol{r}_i(0)-\boldsymbol{r}_j(\tau)]\}\rangle \tag{4.4}$$

with $S(q)$ the static structure factor. The indices recognize a potential coupling between particles i and j directly through the particle pair potential and indirectly through hydrodynamic interactions.

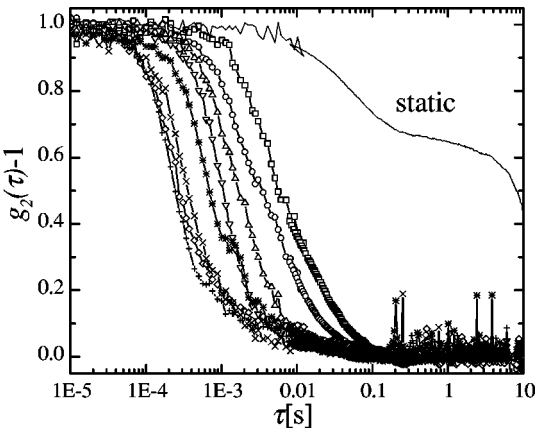

FIG. 4. A comparison of the autocorrelation function with forcing at various frequencies (——, 0 Hz; □, 0.4 Hz; ○, 0.6 Hz; △, 0.8 Hz; ▽, 1.0 Hz; ◇, 2.0 Hz; +, 3.0 Hz; ×, 4.0 Hz; and *, 5.0 Hz). Note that the slow relaxation of the sample cannot significantly affect the rheological measurements.

We measure the displacement of particles rotating with the fluid along with the normal Brownian fluctuations $\boldsymbol{r}_j^d(\tau)$,

$$g_1(q,\tau)=\frac{1}{NS(q)}\sum_{i,j=0}^{N}\langle\exp\{i\boldsymbol{q}\cdot[\boldsymbol{r}_i(0)-\boldsymbol{r}_j^d(\tau)-\Lambda(\omega)\sin\omega\tau\boldsymbol{e}_z\times\boldsymbol{r}_j(0)]\}\rangle. \tag{4.5}$$

If the sample were a rigid solid with $\boldsymbol{r}_j^d=\boldsymbol{r}_j(0)$ and $\Lambda=1$, $g_1(q,\tau)$ would be completely correlated at the inverse of the driving frequency or $\omega\tau=2\pi$ and would follow the shape of the forcing, i.e., sinusoidal. Since our sample fluctuates and deforms and we ensemble-average by superimposing a slow rotation onto the oscillation, crystallites return close but not exactly to their original positions after one oscillation and $g_1(q,2\pi/\omega)<1$. The rates of diffusion and steady rotation for ensemble averaging are much slower than the oscillations and, therefore, affect the primary decay as shown in Fig. 4 very little. At times 10^2-10^3 longer where $\omega\tau=2\pi$, the peak representing the completion of a full oscillation is evident in Fig. 5(a) but is highly attenuated by these processes. Thus our primary interest lies in the decorrelation of the signal by rotation at short times for which $\Lambda(\omega)\sin\omega\tau\approx\Lambda(\omega)\omega\tau\gg|\boldsymbol{r}_j^d(\tau)-\boldsymbol{r}_i(0)|/|\boldsymbol{r}_j(0)|$, so that contributions from Brownian motion and ensemble averaging can be ignored.

For small-amplitude oscillations, the intensity at a Bragg angle is essentially constant. The Bragg reflection dominates the autocorrelation function at this angle and suppresses the decay due to oscillatory shear. Off a Bragg angle, we can determine the decay of the autocorrelation function due to the sample response, though the intensity is much weaker. Therefore, we measure the autocorrelation function at different driving frequencies at a scattering angle just off the main Bragg peak and plot versus $\omega\tau$ to determine the dependence of the rate of decay on frequency. The detector views the center of the sample, sensing the motion propagated inward from the boundaries and, therefore, the bulk rheological properties of the whole sample. Table I summarizes the concentrations and phases of our samples.

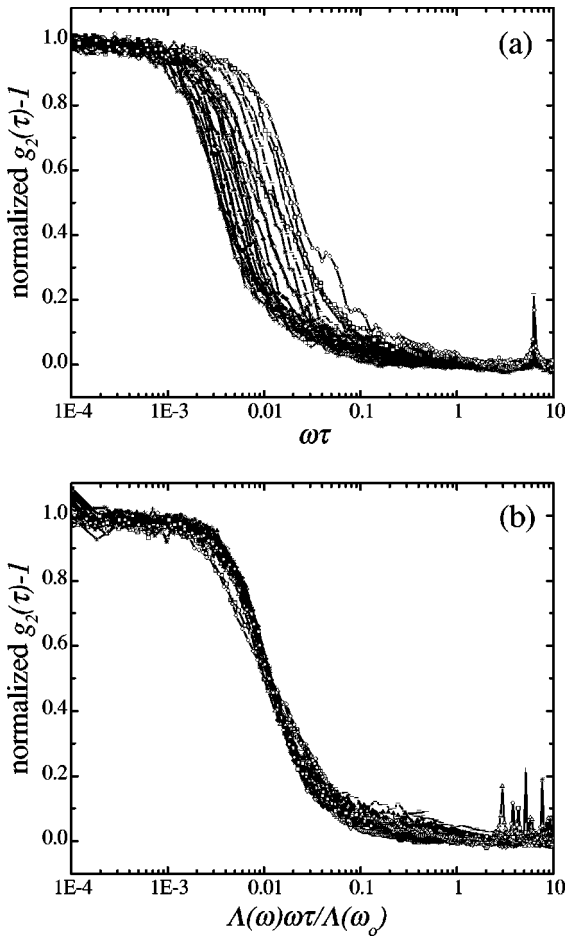

FIG. 5. Autocorrelation functions at driving frequencies between 0.4 to 5.0 Hz in increments of 0.2 Hz are plotted with the delay time either not scaled (a) or scaled (b) to superimpose the responses of sample 4 STS-83 at $\theta=15°$ to oscillatory shear. Note that the decay at the two lowest frequencies (□, 0.4 Hz; ○, 0.6 Hz) is a bit broader than the others, which form a master curve after scaling the delay time.

V. RESULTS

The arguments above lead us to expect the autocorrelation function to decay monotonically with $\Lambda(\omega)\omega\tau$, where $\Lambda(\omega)$ is the frequency-dependent amplitude of rotation in the scattering volume, i.e., the center of the cell, that reflects the viscoelastic properties of the crystal as illustrated by Eq. (3.14). To deduce these properties from the measurement requires extracting $\Lambda(\omega)$ from the decay in the normalized autocorrelation functions, e.g., in Fig. 5(a), via two simple steps. The first step is to superimpose the correlation functions for each frequency ω_i with $t>0$ onto that for the lowest frequency ω_o by plotting versus $\Lambda(\omega_i)\omega_i\tau/\Lambda(\omega_o)$ with the scale factor $\Lambda(\omega_i)/\Lambda(\omega_o)$ chosen for this purpose. Since the decay at the two lowest frequencies is a bit broader than the others [cf. the curves that fall below the other for $\Lambda(\omega_i)\omega_i\tau/\Lambda(\omega_o)<0.01$], we force the collapse at $g_2-1=0.5$ [Fig. 5(b)]. The second and final step is to select $\Lambda(\omega_o)$, G', and η' to obtain the best possible superposition of $\Lambda(\omega)$ versus ω from the measurements with the predictions from Eq. (3.14). This is relatively straightforward, because the resonance frequency primarily determines the modulus with the amplitude or width of the resonance setting the dynamic viscosity.

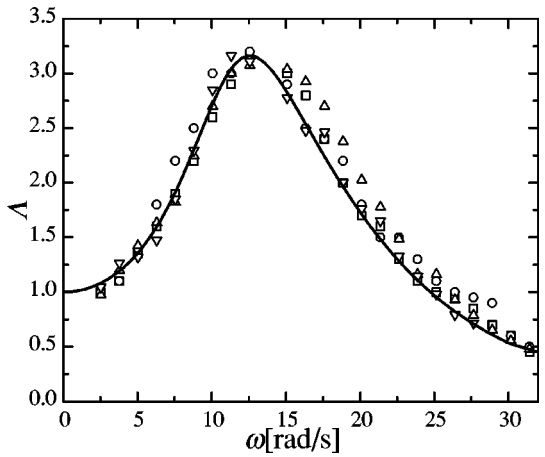

FIG. 6. Resonant response of sample 4 STS-94 at various angles under gravity (▽, KSC, $\theta=15°$) and microgravity (□, STS-94, $\theta=15°$; ○, STS-94, $\theta=30°$; △, STS-83, $\theta=15°$) vs driving frequency compared with the frequency-independent model with $r=0$, $h=1.0$, and $\zeta=0.135$ (——).

The response of sample 4 as a function of driving frequency shown in Fig. 6 for measurements in normal gravity and microgravity environments clearly exhibits the result of this process. The resonance at 12.5 rad/s suggests $G'\cong\rho(12.5R/5.1)^2=0.56$ Pa from (3.2) and Fig. 3, while the peak amplitude of 3.3 indicates a dynamic viscosity of $\eta'=0.12R\sqrt{\rho G'}=0.027$ Pa s from Eq. (3.3) and Fig. 3. The final values result from adjusting these estimates to better fit the full curve. Note that in Fig. 6 the theoretical model describes the full experimental curve fairly well and samples crystallized under gravity exhibit the same resonance as the

TABLE I. Sample descriptions and results for the high-frequency shear modulus and dynamic viscosity in both normal and microgravity environments.

			Gravity		Microgravity	
Sample	ϕ	Phase	$G'_\infty a^3/kT$	η'_∞/μ	$G'_\infty a^3/kT$	η'_∞/μ
2	0.505	coexistence	3.3±1.0	14.1±3.0		
3	0.528	coexistence			4.0±1.0	15.6±3.9
4	0.552	crystal	5.8±0.8	18.8±5.8	5.8±0.8	18.8±4.3
5	0.575	crystal	9.8±3.0	24.5±7.9	9.4±2.0	24.1±5.2
6	0.599	crystal	11.6±3.6	28.8±15		
7	0.622	near glassy	18.1±6.0	44.5±20		

microgravity samples, suggesting that the crystal structure and crystallite size do not affect the bulk rheological properties beyond the experimental error.

The model treats the crystal as a linear viscoelastic solid with constant viscosity and modulus, whereas nonlinearity often sets in at relatively low strains and even crystals exhibit relaxations that cause the moduli to vary with frequency. Thus before analyzing the rheological properties, we need to assess the linearity and the frequency regime of our measurements.

A. Linear regime

For most viscoelastic materials, the response becomes nonlinear above a strain amplitude ϵ_c beyond which the storage modulus generally decreases. Below ϵ_c, in the linear regime, Brownian fluctuations can restore the crystal structure, energy is stored, and the storage modulus remains constant at a fixed frequency. Above ϵ_c, the crystal structure is deformed plastically, energy is dissipated, and the storage modulus decreases.

Shikata and Pearson, Jones, and Frith *et al.* all checked linearity on metastable hard sphere fluids. Shikata and Pearson [6] report a linear response for $\epsilon_c < 0.1$ for their disordered dispersions of 12–450 nm diameter silica in glycerol and ethylene glycol mixtures for $\phi = 0.32 - 0.56$. Jones *et al.* [42] performed measurements on 49 nm diameter silica spheres in high boiling hydrocarbon medium and found $\epsilon_c = 0.03$ for $\phi = 0.586 - 0.667$. For 475 nm PMMA-PHSA in decalin, Frith *et al.* [43] determined that $\epsilon_c = 0.003$ for $\phi = 0.624$ and 0.02 for $\phi = 0.595$, indicating that ϵ_c decreases with increasing concentration. They also noted that nonlinearity first becomes apparent in the loss modulus rather than the storage modulus, with G'' passing through a maximum.

Our instrument imposed oscillations at a fixed amplitude of 1.5° ($\gamma \sim 0.026$). With the known shear modulus and dynamic viscosity, we calculate the strain,

$$\epsilon(r) = \gamma\left(\frac{\partial u_\theta}{\partial r} - \frac{u_\theta}{r}\right), \tag{5.1}$$

at the resonant frequency for sample 4 and find that the greatest strain occurs at the wall. The strain at the wall vs frequency plotted in Fig. 7 for the same sample reaches a maximum strain near the resonance frequency and does not exceed 0.10. Thus our measurements fall in the linear regime according to Shikata and Pearson's criterion but not Jones or Frith *et al.*'s measurements. Frith *et al.* may be the best comparison because their particles most closely resemble ours, but a crystal should tolerate greater strains than a disordered fluid before deforming plastically. Therefore, the critical strain for the fluid only represents a lower limit for the crystal.

We do not perform a direct linearity check, but instead take Bragg images before and after the rheology measurement (Fig. 8). In the linear region, the oscillatory shear mode is nondestructive. The angular averaged Bragg images for samples 3, 4, and 5 from STS-94 before and after the rheology measurement are almost identical, suggesting that the measurement did not affect the structure of the suspension and was in the linear regime. In fact, samples 4 and 5 seem to have increased order, yielding higher intensity Bragg peaks after the measurement, possibly due to shear alignment.

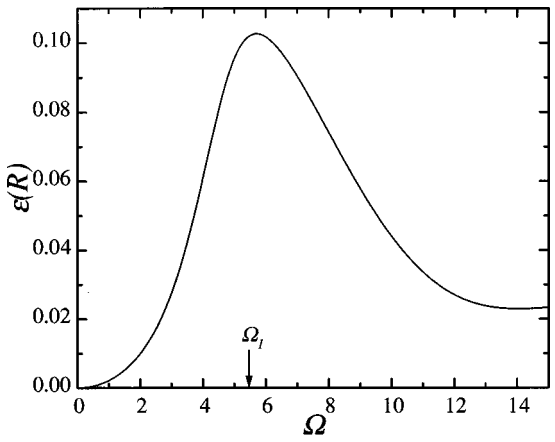

FIG. 7. The frequency dependence of the strain $\epsilon(R)$ with $\zeta = 0.138$ at the container wall for sample 4 STS-94 oscillating with an amplitude of $\pm 1.5°$ shows the greatest strain near the resonant frequency.

B. High-frequency regime

In an oscillatory shear, the frequency scales with the short-time self-diffusion coefficient $D_s^o(\phi)$ because, for small departures from equilibrium, particles need only diffuse a distance small relative to the lattice spacing to relax back to equilibrium. For fluid phases, D_s^o decreases with concentration from the Stokes-Einstein value D_o at infinite dilution. Ottewill and Williams [44] employed 170 nm diameter poly(vinyl acetate) spheres as tracers for 166 nm diameter PMMA-PHSA spheres in a mixture of *cis/trans*-decalin to find $D_s^o(0.50)/D_o = 0.20$ and $D_s^o(0.55)/D_o = 0.15$ for the metastable fluid. Particles ordered onto a crystal lattice are more free to fluctuate than in a disordered fluid, so D_s^o of a crystal should exceed that of a metastable fluid at a fixed concentration. The dimensionless frequency at $\phi = 0.55$ and $\omega_1 = 4\pi$ rad/s, $a^2\omega_1/D_s^o(\phi) \sim 27$, suggests that the measurements lie near or in the high-frequency regime. Alternatively, assuming

$$\frac{D_s^o(\phi)}{D_o} = \frac{\mu}{\eta_\infty'(\phi)} \tag{5.2}$$

for the crystal, which is not precise but is at least within a factor of 2, and employing the high-frequency viscosities of Nunan and Keller (1984) determines a lower bound of $(a^2\omega_1/D_o)(\eta_\infty'/\mu) \sim 22$, just slightly less than the dimensionless frequency determined with the short-time self-diffusion coefficient. Thus, we cannot access the low-frequency regime because of our large particle size.

C. Shear moduli

For hard spheres the dimensionless shear moduli, scaled on the thermal energy density as Ga^3/kT, should depend only on ϕ and the dimensionless frequency $a^2\omega/D_o$. Our elastic moduli G' (Fig. 9 and Table I) are comparable to the

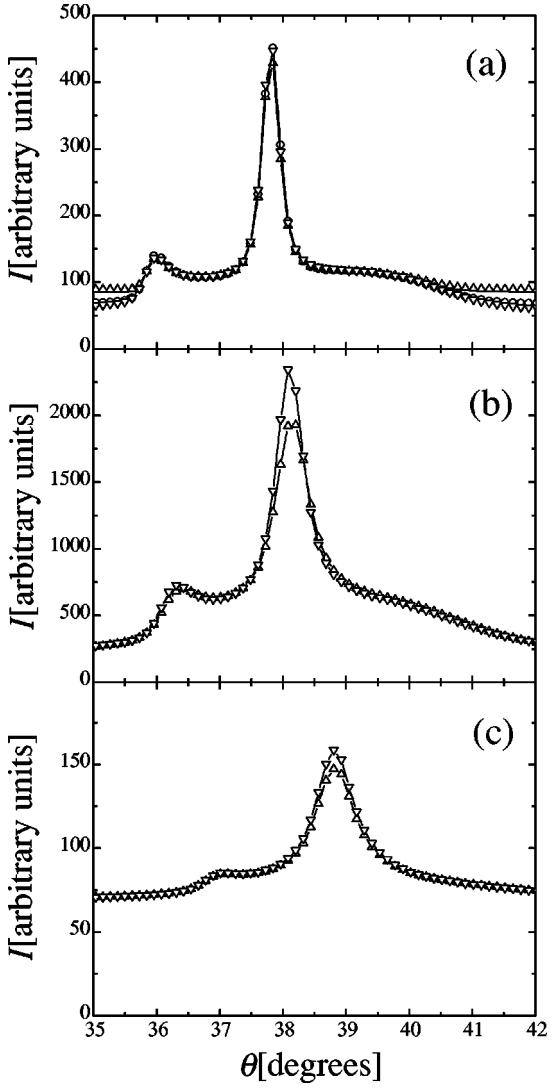

FIG. 8. Bragg scattering from samples 3 (a), 4 (b), and 5 (c) on STS-94 remains nearly the same before (△), during (○), and after (▽) the rheological measurement, suggesting that the rheological properties are obtained in the linear regime.

static shear moduli calculated by Frenkel and Ladd [31] for a fcc crystal and well below the high-frequency moduli from Lionberger and Russel's nonequilibrium theory [45] and Shikata and Pearson's measurements [6] for the metastable fluid. The static modulus is an equilibrium property that is unaffected by hydrodynamic interactions, unlike the high-frequency modulus, which measures the instantaneous response to a strain. Both hydrodynamic interactions and the nonequilibrium structure cause the high-frequency modulus to always exceed the static modulus. Our results seem reasonable, as they lie between the static modulus for a fcc crystal and the high-frequency modulus for the metastable fluid. While our moduli lie just slightly above Frenkel and Ladd's predictions, the difference is not necessarily significant as indicated by the error bars. Thus, our results agree qualitatively with van der Vorst *et al.*'s [15,25] measurements on aqueous latex dispersions in not deviating much from the static modulus, though at a relatively high frequency.

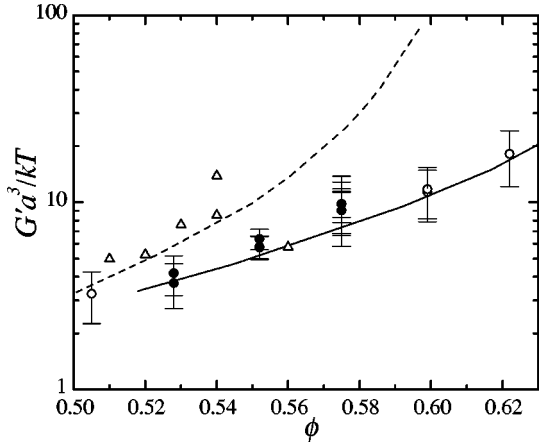

FIG. 9. The shear moduli of our colloidal crystals measured in gravity (○) and microgravity (●) and determined with frequency-independent rheological properties compared with measurements and theory for the high-frequency moduli of the metastable fluid (△, Shikata and Pearson [6]; – – –, Lionberger and Russel [45]), and Frenkel and Ladd's prediction ([31], ——) for the static moduli of a fcc crystal.

D. Dynamic viscosity

The dynamic viscosity scaled by the solvent viscosity μ (Fig. 10 and Table I) increases from about 14 to 44.5 for $0.505 \leqslant \phi \leqslant 0.622$. Our earlier estimates suggest the measurements to be in the high-frequency limit. Therefore, we include for comparison the high-frequency viscosities for a perfect fcc hard sphere crystal, calculated by Nunan and Keller [32], and a disordered metastable hard sphere fluid, measured by Shikata and Pearson [6] and van der Werff *et al.* [7]. Brownian motion of particles about the lattice sites in our crystals causes closer interactions and should increase the viscosity above the lower bound set by the perfect crystal, but not above the value for the disordered fluid. The

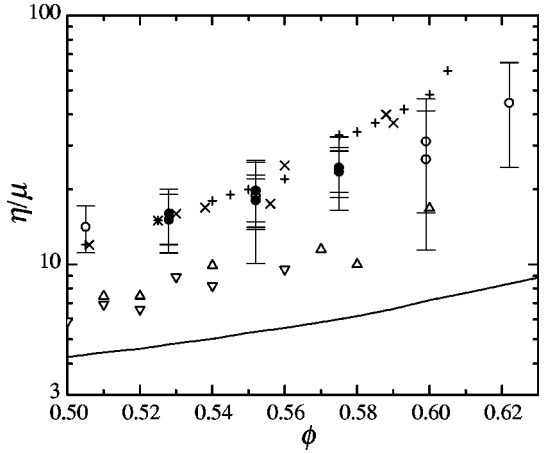

FIG. 10. The dynamic viscosity of our colloidal crystals measured in gravity (○) and microgravity (●) determined with frequency-independent rheological properties compared with measurements of the high shear (+, van der Werff and de Kruif [4]; ×, Woods and Krieger [46]) and high-frequency (△, Shikata and Pearson [6]; ▽, van der Werff *et al.* [7]) viscosities for the metastable fluid and Nunan and Keller's theory ([32], ——) for the effective viscosity of an unstrained fcc crystal.

coincidence between our data and the high shear viscosities for disordered hard sphere fluids measured by van der Werff and de Kruif [4] and Woods and Krieger [46] suggests that nonlinearity might be the culprit. However, we should first check that the assumption of a frequency independent viscosity is not at fault.

A viscoelastic solid with one relaxation time has the frequency-dependent shear modulus and dynamic viscosity,

$$\frac{G'}{G_o} = 1 + \frac{G'_\infty - G_o}{G_o} \frac{(\omega\tau_o)^2}{1+(\omega\tau_o)^2} \tag{5.3}$$

and

$$\frac{\eta'}{\eta'_\infty} = \frac{G''}{\omega} = 1 + \frac{\eta'_o - \eta'_\infty}{\eta'_\infty} \frac{1}{1+(\omega\tau_o)^2} \tag{5.4}$$

with the relaxation time

$$\tau_o = \frac{\eta'_o - \eta'_\infty}{G'_\infty - G_o}. \tag{5.5}$$

We fix the static shear modulus to Frenkel and Ladd's predictions for a fcc crystal and the high-frequency modulus to that extracted from our measurements without accounting for the frequency dependence. If we set the low-frequency viscosity to Nunan and Keller's prediction, no high-frequency viscosity would fit our data. Thus the high- and low-frequency viscosities must be adjusted simultaneously to obtain a reasonable fit. With η'_o fixed, increasing η'_∞ moves the maximum amplitude to lower frequencies and decreases the tail of the resonance. On the other hand, with η'_∞ fixed, increasing η'_o decreases the initial curvature, moves the maximum amplitude to higher frequencies, and decreases the tail of the resonance. Figure 11 summarizes the high- and low-frequency viscosities obtained from the frequency-dependent model. Including the frequency dependence lowers η'_∞ a bit, but our values still lie above measurements on the metastable fluid and slightly below the low-frequency viscosities. Nonetheless, the viscoelastic solid with one relaxation time suggests that our dispersion acts solidlike ($\tan\delta \sim 0.8$) at the resonant frequency.

The high value for the high-frequency dynamic viscosity may result from nonlinear effects; as Frith *et al.* [43] noted, measurements may be in the linear regime for the storage modulus but in the nonlinear regime for the loss modulus. If our strain amplitude occurs near the maximum in the loss modulus, that would result in a higher value for the dynamic viscosity. Thus, the similarity between our values for η'_∞ and the measured values for η_∞ (Figs. 10 and 11) may be significant.

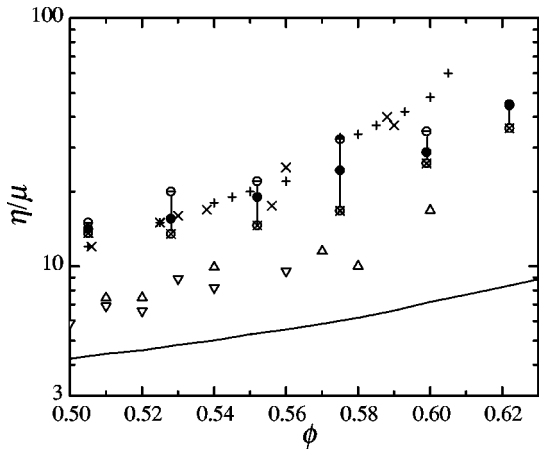

FIG. 11. Including frequency-dependent rheological properties in our model lowers the high-frequency viscosity ($\otimes$) of our colloidal crystals but still seems high compared with measurements of the high-frequency viscosities for the metastable fluid (Shikata and Pearson [6]; van der Werff *et al.* [7]). $\odot$ represents the average of the high-frequency viscosity measured in gravity and microgravity and determined from the frequency-independent rheological properties, while $\ominus$ represents the low-frequency viscosity. See Fig. 10 for other symbol definitions.

VI. CONCLUSIONS

These data represent the first measurements of the viscoelastic properties of nonaqueous hard sphere colloidal crystals. Detecting the resonance with dynamic light scattering gives values of the high-frequency shear modulus of our colloidal hard spheres in quantitative agreement with predictions of the static shear modulus from computer simulations. However, the high-frequency dynamic viscosity is too high, even when frequency dependence associated with a single relaxation time is incorporated. Though effectively in the linear regime for the shear modulus, our measurements may be nonlinear for the loss modulus, therefore producing high values for η'_∞.

ACKNOWLEDGMENTS

We would like to thank the PHaSE team at NASA Lewis Research Center in Cleveland, OH for their work on the instrument, and Sal Torquato for his help in determining the orientationally averaged modulus. This research was funded by a NASA grant (No. NAG 3-1762) and the Graduate Student Researchers Program.

[1] P. Pusey and W. van Megen, in *An Exxon Monograph: Physics of Complex and Supermolecular Fluids*, edited by S. A. Safran and N. A. Clark (John Wiley & Sons, New York, 1987), pp. 673–698.
[2] G. Batchelor, J. Fluid Mech. **83**, 97 (1977).
[3] J. Mewis, W. Frith, T. Strivens, and W. Russel, AIChE. J. **35**, 415 (1989).
[4] J. van der Werff and C. de Kruif, J. Rheol. **33**, 421 (1989).
[5] I. Krieger, Adv. Colloid Interface Sci. **3**, 111 (1972).
[6] T. Shikata and D. Pearson, J. Rheol. **38**, 601 (1994).
[7] J. van der Werff, C. de Kruif, C. Blom, and J. Mellema, Phys. Rev. A **39**, 795 (1989).
[8] W. Frith, T. Strivens, and J. Mewis, J. Colloid Interface Sci. **139**, 55 (1990).

[9] P. D'Haene, *Rheology of Polymerically Stabilized Suspensions* (Katholieke Universiteit, Leuven, Netherlands, 1992).
[10] L. Chen, B. Ackerson, and C. Zukoski, J. Rheol. **38**, 193 (1994).
[11] M. Chow and C. Zukoski, J. Rheol. **39**, 33 (1995).
[12] D. Benzing and W. Russel, J. Colloid Interface Sci. **83**, 178 (1981).
[13] R. Buscall, J. Goodwin, M. Hawkins, and R. Ottewill, J. Chem. Soc., Faraday Trans. 1 **78**, 2873 (1982).
[14] H. Lindsay and P. Chaikin, J. Chem. Phys. **76**, 3774 (1982).
[15] B. van der Vorst, D. van den Ende, and J. Mellema, J. Rheol. **39**, 1183 (1995).
[16] R. Crandall and R. Williams, Science **198**, 293 (1977).
[17] E. Dubois-Violette, P. Pieranski, F. Rothen, and L. Strzelecki, J. Phys. (Paris) **41**, 369 (1980).
[18] M. Joanicot, M. Jorand, P. Pieranski, and F. Rothen, J. Phys. (Paris) **45**, 1413 (1984).
[19] J. Joanny, J. Colloid Interface Sci. **71**, 622 (1979).
[20] S. Mitaku, T. Ohtsuki, K. Enari, A. Kishimoto, and K. Okano, Jpn. J. Appl. Phys., Part 1 **17**, 305 (1978).
[21] S. Mitaku, T. Ohtsuki, and K. Okano, Jpn. J. Appl. Phys., Part 1 **19**, 439 (1980).
[22] P. Chaikin, J. di Meglio, W. Dozier, H. Lindsay, and D. Weitz, in *Physics of Complex and Supermolecular Fluids*, edited by S. A. Safran and N. A. Clark (John Wiley & Sons, New York, 1987), pp. 65–81.
[23] H. Lindsay and P. Chaikin, J. Phys. (Paris) **46**, C3 (1985).
[24] J. Goodwin, T. Gregory, J. Miles, and B. Warren, J. Colloid Interface Sci. **97**, 488 (1984).
[25] B. van der Vorst, D. van den Ende, and J. Mellema, Physica B **228**, 180 (1996).
[26] C. Blom, J. Mellema, J. Lopulissa, and A. Reuvers, Colloid Polym. Sci. **262**, 397 (1984).
[27] T. Palberg, J. Kottal, T. Loga, H. Hecht, E. Simnacher, F. Falcoz, and P. Leiderer, J. Phys. III **4**, 457 (1994).
[28] R. Buscall, J. Goodwin, M. Hawkins, and R. Ottewill, J. Chem. Soc., Faraday Trans. 1 **78**, 2873 (1982).
[29] W. Russel and D. Benzing, J. Colloid Interface Sci. **83**, 163 (1981).
[30] M. Jorand, E. Dubois-Violette, B. Pansu, and F. Rothen, J. Phys. (Paris) **49**, 1119 (1988).
[31] D. Frenkel and A. Ladd, Phys. Rev. Lett. **59**, 1169 (1987).
[32] K. Nunan and J. Keller, J. Fluid Mech. **142**, 269 (1984).
[33] S. Phan, Ph.D. dissertation, Princeton University, Princeton, NJ, 1998.
[34] S. Phan, W. Russel, Z. Cheng, J. Zhu, P. Chaikin, and J. Dunsmuir, Phys. Rev. E **54**, 6633 (1996).
[35] P. Bolhuis and D. Kofke, Phys. Rev. E **54**, 634 (1996).
[36] J. Zhu, M. Li, R. Rogers, W. Meyer, R. Ottewill, STS-73 Space Shuttle Crew, W. Russel, and P. Chaikin, Nature (London) **387**, 883 (1997).
[37] L. Woodcock, Nature (London) **385**, 141 (1997).
[38] P. Bolhuis, D. Frenkel, S. Mau, and D. Huse, Nature (London) **388**, 235 (1997).
[39] P. Pusey, W. van Megen, W. Bartlett, B. Ackerson, J. Ravity, and S. Underwood, Phys. Rev. Lett. **63**, 2753 (1989).
[40] W. Russel, P. Chaikin, J. Zhu, W. Meyer, and R. Rogers, Langmuir **13**, 3871 (1997).
[41] C. Lant, A. Smart, D. Cannell, W. Meyer, and M. Doherty, Appl. Opt. **36**, 7501 (1997).
[42] D. Jones, B. Leary, and D. Boger, J. Colloid Interface Sci. **147**, 479 (1991).
[43] W. Frith, J. Mewis, and T. Strivens, Powder Technol. **51**, 27 (1987).
[44] R. Ottewill and N. Williams, Nature (London) **325**, 232 (1987).
[45] R. Lionberger and W. Russel, J. Rheol. **38**, 1885 (1994).
[46] M. Woods and I. Krieger, J. Colloid Interface Sci. **34**, 91 (1970).